Strain Engineering: Perfecting Freestanding Perovskite Oxide Fabrication

Yun, Shinhee; le Cozannet, Thomas Emil; Christoffersen, Christina Høgfeldt; Brand, Eric; Jespersen, Thomas Sand; Pryds, Nini

Published in:
Small

Link to article, DOI:
10.1002/smll.202310782

Publication date:
2024

Document Version
Version created as part of publication process; publisher's layout; not normally made publicly available

RESEARCH ARTICLE

NANO · MICRO small
www.small-journal.com

Strain Engineering: Perfecting Freestanding Perovskite Oxide Fabrication

Shinhee Yun, Thomas Emil le Cozannet, Christina Høgfeldt Christoffersen, Eric Brand, Thomas Sand Jespersen, and Nini Pryds**

Freestanding oxide membranes provide a promising path for integrating devices on silicon and flexible platforms. To ensure optimal device performance, these membranes must be of high crystal quality, stoichiometric, and their morphology free from cracks and wrinkles. Often, layers transferred on substrates show wrinkles and cracks due to a lattice relaxation from an epitaxial mismatch. Doping the sacrificial layer of $Sr_3Al_2O_6$ (SAO) with Ca or Ba offers a promising solution to overcome these challenges, yet its effects remain critically underexplored. A systematic study of doping Ca into SAO is presented, optimizing the pulsed laser deposition (PLD) conditions, and adjusting the supporting polymer type and thickness, demonstrating that strain engineering can effectively eliminate these imperfections. Using $SrTiO_3$ as a case study, it is found that $Ca_{1.5}Sr_{1.5}Al_2O_6$ offers a near-perfect match and a defect-free freestanding membrane. This approach, using the water-soluble $Ba_x/Ca_xSr_{3-x}Al_2O_6$ family, paves the way for producing high-quality, large freestanding membranes for functional oxide devices.

1. Introduction

Since the 2016 breakthrough in producing single crystalline perovskite oxide membranes, there has been extensive research into freestanding transition metal oxides.[1–8] These studies aim to harness their potential for functional oxide device applications. The freestanding membrane platform offers the unique ability to control strain continuously. This capability has opened doors to modifying properties in functional materials like dielectric, ferroelectric, and magnetic oxides through strain effects.[9–15] R. Xu and team found that applying uniaxial strain to centrosymmetric $SrTiO_3$ (STO) membranes induces a non-centrosymmetric phase with ferroelectric properties, resulting in stripe domains of in-plane polarizations.[16] Reports also suggest that strain can control electromechanics, magnetization states, and electronic conductivity, laying the groundwork for device applications.[10,17,18] Lately, there has been growing interest in exploring interface phenomena in twisted membranes.[2] In all of these studies, it is crucial to fabricate membranes with sharp interfaces and free from wrinkles and cracks. Membrane fabrication using wet etching typically involves two steps: 1) material synthesis and 2) membrane transfer with a polymer.[19]

While the synthesis step can produce stoichiometric single-crystalline thin films, the intrinsic epitaxial strain between the film and the sacrificial layer below can compromise the final quality of freestanding membranes. Releasing a highly strained film from its clamped sacrificial layer can create significant stress gradients, especially near the boundary between released and unreleased areas. These stress gradients can lead to cracks along crystal planes or wrinkles.[20,21] The stress gradient magnitude is tied to the mismatch between the film and the water-soluble sacrificial layers. Minimizing this mismatch can reduce stress during release, resulting in fewer cracks or wrinkles in the final released membrane. One way to achieve this is by adjusting the lattice parameter of the water-soluble layer, such as by doping Ca or Ba into Sr-sites in $Sr_3Al_2O_6$ (SAO) [12,22–25]

Structural distortions in freestanding membranes due to the mismatch between the layers have not been well-documented yet.[17,26] However, the relation between mismatches and defects can be inferred intuitively. For a tensile-strained layer atop a sacrificial layer, the membrane tends to shrink during release with the etchant. This is because its natural lattice parameter is smaller than the water-soluble layer. If the stress during this shrinking process is too high, the membrane can be fractured. Conversely, the released layer expands for a compressive-strained layer, leading to wrinkles beneath the supporting polymer layer. This expansion occurs as the lattice parameter reverts to its original size, which is larger than the sacrificial layer. The wrinkle's curvature is influenced by the degree of compressive strain and the layer thickness.

Interestingly, another strain effect is observed in heterostructures composed of two different epitaxial layers – strain gradient.

S. Yun, T. E. le Cozannet, C. H. Christoffersen, E. Brand, T. S. Jespersen, N. Pryds
Department of Energy Conversion and Storage
Technical University of Denmark (DTU)
Fysikvej, 310, Kgs. Lyngby 2800, Denmark
E-mail: shiyu@dtu.dk; nipr@dtu.dk

The ORCID identification number(s) for the author(s) of this article can be found under https://doi.org/10.1002/smll.202310782

DOI: 10.1002/smll.202310782

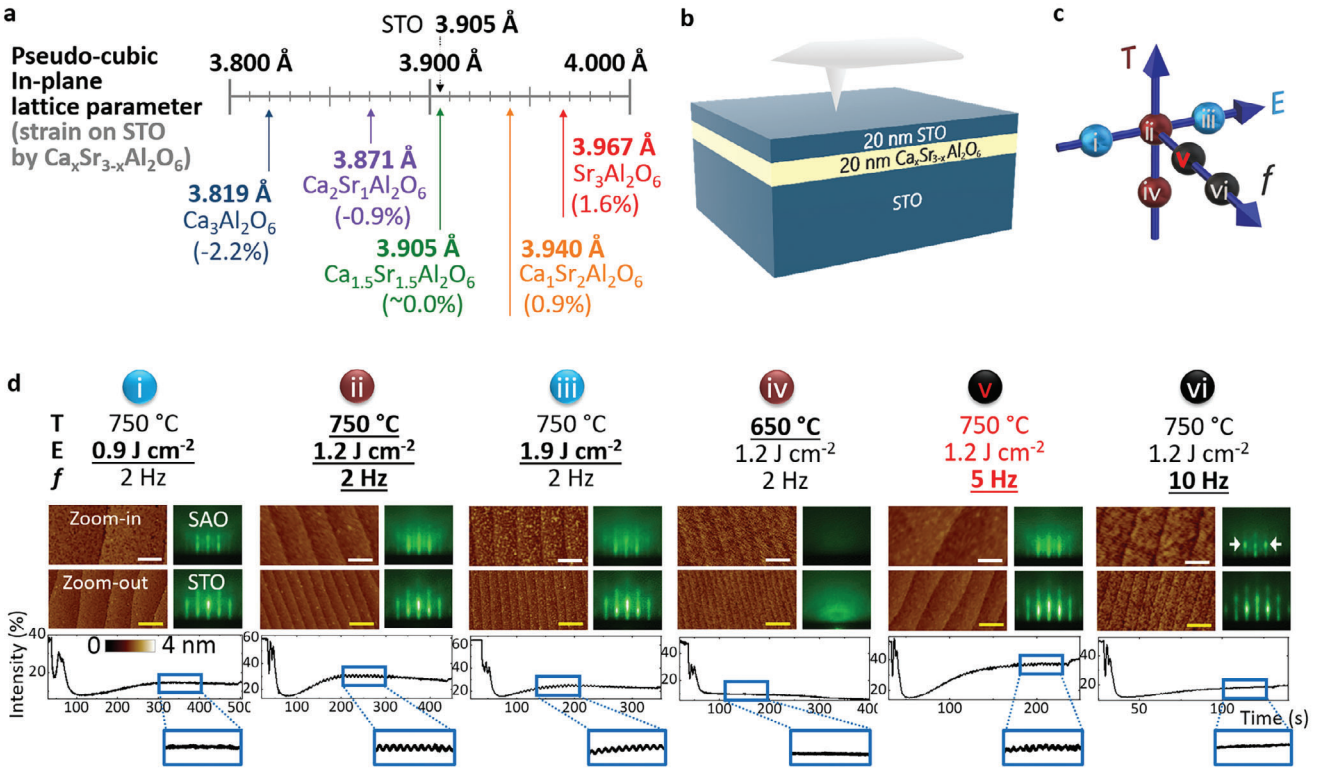

Figure 1. provides a comprehensive overview of the strain in the STO epitaxial layer on CSAO and the PLD of SAO under various conditions. a) Displays the pseudo-cubic in-plane lattice parameters of both CSAO and STO. The strain values for the STO layers on each CSAO are marked alongside the lattice parameters. b) A schematic illustration of the target layer (STO) and the sacrificial layer (CSAO) grown on an STO (001) substrate. c) A schematic detailing the PLD conditions that were tested. These conditions are plotted on three axes representing substrate temperature (*T*), laser energy density (*E*), and the repetition rate of the laser (*f*). d) The surface morphology of the developed STO/CSAO/STO (001) is shown, accompanied by RHEED patterns and the time-dependent intensity of the specular spots for each deposition condition corresponding to the conditions in part (c). The AFM image includes a white scale bar representing 400 nm, while a yellow scale bar indicates 1 µm. The optimal PLD condition for SAO is highlighted in red. The reference condition, which is (ii) centered in (c), is in bold and underlined, and the changed conditions in (i) and (iii)–(vi) compared to (ii) are also marked in bold and underlined.

Due to the strain gradient along the heterostructure thickness, the released heterostructure can self-roll.[27–31] Such rolls have potential applications as nanowires in devices. While certain devices can benefit from deformed freestanding membranes by amplifying or diminishing specific phenomena, many applications, such as field effect transistors, electrolytes, and spintronic devices, require flat and well-defined surfaces of the membranes. Although these membranes can be produced on a macroscopic millimeter scale, they often have wrinkles and cracks on the microscopic scale, which significantly limits their usable area for experiments and applications. Therefore, a comprehensive study has yet to be conducted to identify the conditions necessary for producing flat, defect-free, and freestanding membranes.

To circumvent the most significant issues associated with the freestanding oxide transfer that arise from cracks and wrinkles during the release process, this paper explores the possibility of adjusting the mismatch between the prototypical oxide STO layer and the water-soluble layer. This is achieved by doping Ca cations into the Sr-sites of the water-soluble SAO, allowing for a modifiable lattice parameter. Additionally, we have conducted a systematic analysis of the crystal structure and the membrane-released features (e.g., sacrificial layer thickness, release time, and type of polymer), aiming for flawless freestanding perovskite oxide membranes. While crucial, detailing the properties of freestanding films falls outside the scope of this paper. Our aim is mainly to provide the conditions required for fabricating, releasing, and transferring high-quality membranes, as evidenced structurally.

2. Results and Discussion

2.1. Optimal PLD Conditions of $Ca_xSr_{3-x}Al_2O_6$ (CSAO) Growth

Epitaxial water-soluble CSAO layers were deposited using PLD on STO (001) single crystals terminated with TiO_2. Depending on the Ca doping ratio, the pseudo-cubic lattice parameter ($a_{pc} = ¼$ a, where a is the lattice parameter of the CSAO unit cell) of CSAO ranges between 3.819 and 3.967 Å.[19] This variation is due to the smaller Ca ions effectively reducing the CSAO lattice parameter when they replace the Sr-sites, as illustrated in **Figure 1a**. Among the CSAO family, fully doped $Ca_3Al_2O_6$ possesses the smallest lattice parameter. Subsequently, 20-nm-thick STO layers were epitaxially grown on these 20-nm-thick CSAO layers, as shown in Figure 1b.

To achieve optimal growth conditions for both CSAO and STO, various deposition conditions were tested initially for SAO. As depicted in Figure 1c, these conditions are represented as (i)–(vi)

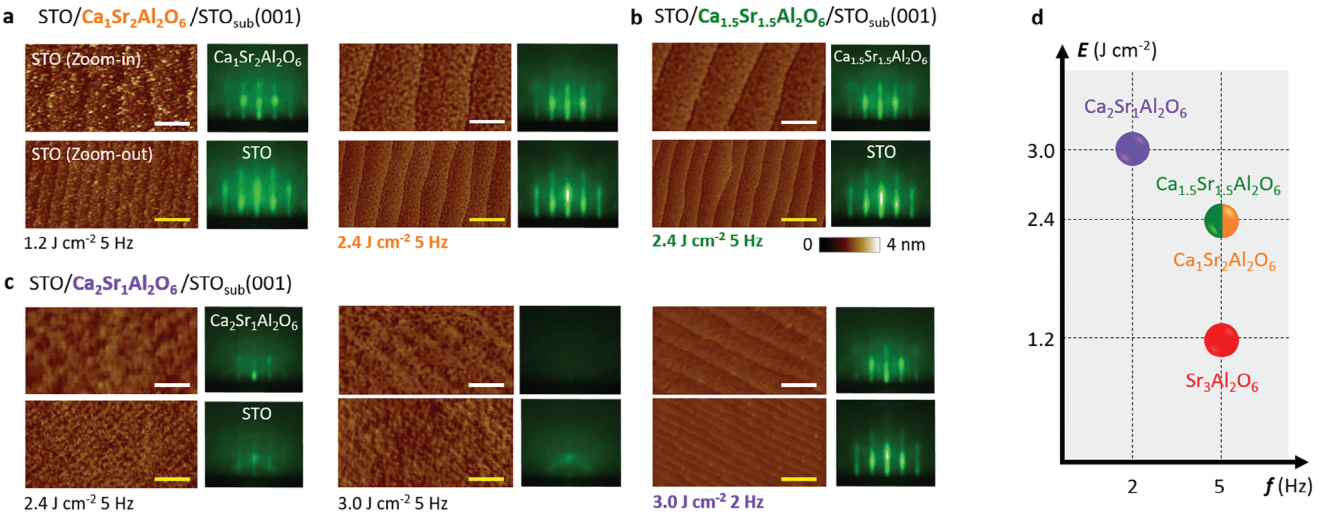

Figure 2. provides a detailed overview of the optimal PLD conditions for the growth of CSAO. a–c) These micrographs display the surface morphologies and in–situ RHEED patterns under varying laser energy densities and repetition rates for the following configurations: STO/$Ca_1Sr_2Al_2O_6$/STO (001) (a), STO/$Ca_{1.5}Sr_{1.5}Al_2O_6$/STO (001) (b), STO/$Ca_2Sr_1Al_2O_6$/STO (001) (c). The optimal conditions for each configuration are emphasized using colors that correspond to the specific doping ratio of CSAO. For clarity in the AFM images, a white scale bar represents 400 nm, while a yellow scale bar indicates 1 µm. d) Plots the optimal conditions of the laser energy density and repetition rate for each CSAO.

and span three different parameters: the substrate temperature, T [°C], the laser energy density, E [J cm^{-2}], and the laser repetition rate, f [Hz]. For each growth condition, Figure 1d shows atomic force microscopic (AFM) images of STO/SAO/STO(001) surfaces, in–situ reflection high energy electron diffraction (RHEED) patterns for both SAO and STO during the growth, and time-dependent intensity of the specular spots. The optimal deposition conditions are reached at point (v), where clear and well-defined streak RHEED patterns are observed for both SAO and STO, coupled with increasing intensity of the RHEED specular spot, which suggests a limited atomic long-range order at the surface. In addition, we note the following: When the SAO layer is grown at a temperature of 650 °C, the RHEED pattern becomes nearly indiscernible due to surface roughness, while the STO pattern exhibits polycrystalline features, i.e., diffraction ring, as seen in Figure 1d(iv). Despite this, the time-dependent RHEED intensity does not show oscillations and gradually fades, even though a subtle step-terrace structure can be discerned in the AFM image. Films grown at a higher laser repetition rate of 10 Hz tend to have a rougher surface (Figure 1d(vi)). The corresponding RHEED patterns reveal transmission spots (see white arrows in panel vi), suggesting the growth of 3D islands. In contrast, depositing at a lower repetition rate, 2 Hz, yields results similar to the optimal condition with decreasing the time-dependent RHEED intensity, as depicted in Figure 1d(ii). Lastly, when either a lower or higher laser energy density is employed (i and iii), the resulting surface appears granular, with transmission spots evident in the RHEED pattern and decreasing intensity of the specular spot with growth time (Figure 1d(i),(iii) bottom panels).

Compared to SAO, the Ca—O bond strength in CSAO is significantly stronger than the Sr—O bond.[32] Thus, a higher laser energy density is required to achieve a stoichiometric plasma plume during the deposition. When the laser energy density of 1.2 J cm^{-2}, previously determined as optimal for SAO, is used for $Ca_1Sr_2Al_2O_6$, it leads to the formation of a secondary phase during the growth process. This is evident in the AFM images and the 3D-island spots in the RHEED patterns, a consequence of non-stoichiometry (**Figure 2**a left). However, when the laser energy density increases to 2.4 J cm^{-2}, high-quality $Ca_1Sr_2Al_2O_6$ and $C_{1.5}Sr_{1.5}Al_2O_6$ are achieved (Figure 2a right,b). For the higher doping ratio, $Ca_2Sr_1Al_2O_6$, the crystalline quality does not improve even with the increased laser energy density, and rough surface morphologies and polycrystalline rings in the RHEED patterns are observed (Figure 2c left and middle). Intriguingly, reducing the laser repetition rate to 2 Hz enhances the crystalline quality, as seen in Figure 2c right panel. This indicates that the robust Ca—O bonding also influences the diffusion dynamics on the surface during the growth phase. With smaller f, the longer time for diffusion promotes layer-by-layer growth mode (Figure 2d). It is important to note that optimized CSAO depositions, characterized by clear RHEED oscillations, indicate optimal layer-by-layer growth conditions for a specific crystal miscut angle. Increasing this miscut angle results in a transition to a 3D island growth mode.

2.2. Epitaxial Strain in STO Layer on CSAO

Figure 3 explores the epitaxial strains of 20-nm-thick STO film on CSAO layers using X-ray diffraction scans. Consider first the θ–2θ scans: Within the vicinity of STO (002), the thickness fringes of both 20 and 50-nm CSAO layers suggest atomically well-defined interfaces of the STO and CSAO layers (Figure 3a,b). Estimating the film thickness using the Kiessig fringes validated the thickness measurements obtained through RHEED. The peak related to the STO (002) of the substrate is clearly seen (black arrow). Also, the positions of the (002) peak of the STO top film are marked by colored circles, which are to be strained to epitaxially match the CSAO. These are paired with similarly colored inverted triangles for the (002) of the CSAO layers. The positions

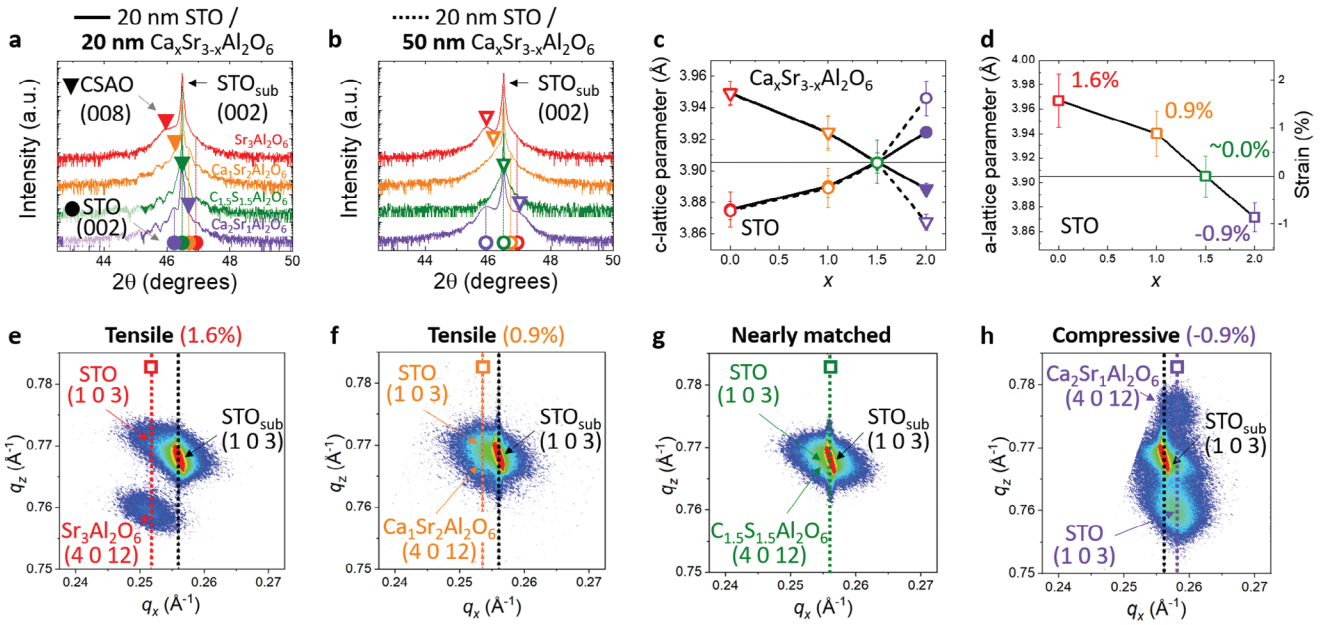

Figure 3. presents a detailed analysis of the X-ray diffractions of the epitaxial STO/CSAO/STO (001) structure. a) Shows the $\theta-2\theta$ scans for the 20-nm-thick STO layers grown on 20-nm-thick CSAO layers. The inverted solid triangles mark the peak positions of the 20-nm-thick CSAO layers, while the solid circles denote the peak positions of the epitaxial STO layers grown on each CSAO layer. b) $\theta-2\theta$ scans for the 20-nm-thick STO layers on 50-nm-thick CSAO layers are displayed. The empty triangles represent the peak positions of the 50-nm-thick CSAO layers, and the empty circles indicate the peak positions of the epitaxial STO layers grown on each CSAO layer. c) Represents the c-lattice parameters of both STO and CSAO, derived from the data in sections (a) and (b) by deconvolution. d) Plots of the a-lattice parameters of STO on the 50-nm-thick CSAO and its corresponding in-plane strains derived from (e) to (h) indicated by empty squares. e–h) RSMs near the Bragg peaks of the 20-nm-thick STO (1 0 3) and the 50-nm-thick CSAO (4 0 12).

of all peaks were deducted by deconvolutions, and the error bars were calculated using the full-width half maximum (FWHM) of the deconvoluted peak. Given that SAO and $Ca_1Sr_2Al_2O_6$ (red and orange inverted triangles) have larger *in-plane* lattice parameters than the STO, the STO layers atop them experience tensile strain (red and orange circles). This results in the STO top-film peaks positioned to the right of the STO_{sub} (002) peak, indicating a compressed *c*-axis parameter. The lattice parameter of $Ca_{1.5}Sr_{1.5}Al_2O_6$ closely matches the STO, causing the peaks of STO (002) and $Ca_{1.5}Sr_{1.5}Al_2O_6$ (002) to overlap with STO_{sub} (002) in the $\theta-2\theta$ scan. For $Ca_2Sr_1Al_2O_6$, which has a smaller lattice parameter than STO_{sub} (purple inverted triangle), the overlying STO layer undergoes *in-plane* compressive strain, leading to an elongated STO *c*-axis lattice parameter (denoted by the purple circle). Notably, a thicker $Ca_2Sr_1Al_2O_6$ layer, like 50 nm, when more relaxed, causes even more elongation of the STO layer along the *c*-axis compared to a 20-nm-thick $Ca_2Sr_1Al_2O_6$ layer, as evidenced by the differing positions of the purple circles in Figure 3a,b. The c-lattice parameters derived from the $\theta-2\theta$ scans in Figure 3a,b are graphically represented in Figure 3c. In this plot, the unique behavior of the highest Ca-doped ratio in CSAO, specifically $Ca_2Sr_1Al_2O_6$, stands out from other CSAOs. This difference is believed to be due to its higher elastic moduli, a result of stronger Ca—O bonding. A 20 nm thick layer of $Ca_2Sr_1Al_2O_6$ is not fully relaxed, while the 20 nm layers of SAO, $Ca_1Sr_2Al_2O_6$, and $Ca_{1.5}Sr_{1.5}Al_2O_6$, are fully relaxed as indicated by their similar c-lattice parameters. This suggests that higher elastic moduli require a thicker layer to achieve full relaxation. Due to the limited intensity of the 20-nm-thick CSAO, Reciprocal Space Maps (RSMs) for the 50-nm-thick CSAO were acquired (Figure 3e-h). It is important to recognize that the thickness required for a fully relaxed layer varies significantly between materials and needs to be optimized for each. In our current experiments, for full relaxation on STO substrates, the thickness threshold is below 20 nm for SAO and $Ca_1Sr_2Al_2O_6$. In contrast, for $Ca_2Sr_1Al_2O_6$, the threshold for full relaxation exceeds 20 nm.

All the STO layers are observed to be fully strained on the CSAO layers. However, all CSAO layers appear to be fully or partially relaxed from the STO_{sub} (002), as indicated by the red and black dashed lines in Figure 3e–h.

The peak positions allowed for the calculation of mismatch strains, which are graphically represented in Figure 3d. The strains are 1.6%, 0.9%, ≈0%, and −0.9% for SAO, $Ca_1Sr_2Al_2O_6$, $Ca_{1.5}Sr_{1.5}Al_2O_6$, and $Ca_2Sr_1Al_2O_6$, respectively. The minimal mismatch with STO is observed in $Ca_{1.5}Sr_{1.5}Al_2O_6$, which displays nearly co-located Bragg peaks, appearing almost as a singular peak in Figure 3g.

2.3. Release and transfer of STO layers from CSAO

Figure 4 shows how the degree of strains influences the release features of the STO layer from the CSAO layers during the introduction of water. A thick (≈100 µm) polymer support (cellulose acetate butyrate (CAB)) was spin-coated on the STO layer on the top (See Experimental Section). The adhesion between the STO and the polymer is an important parameter that can be compromised due to an alteration in the STO strain state when it is

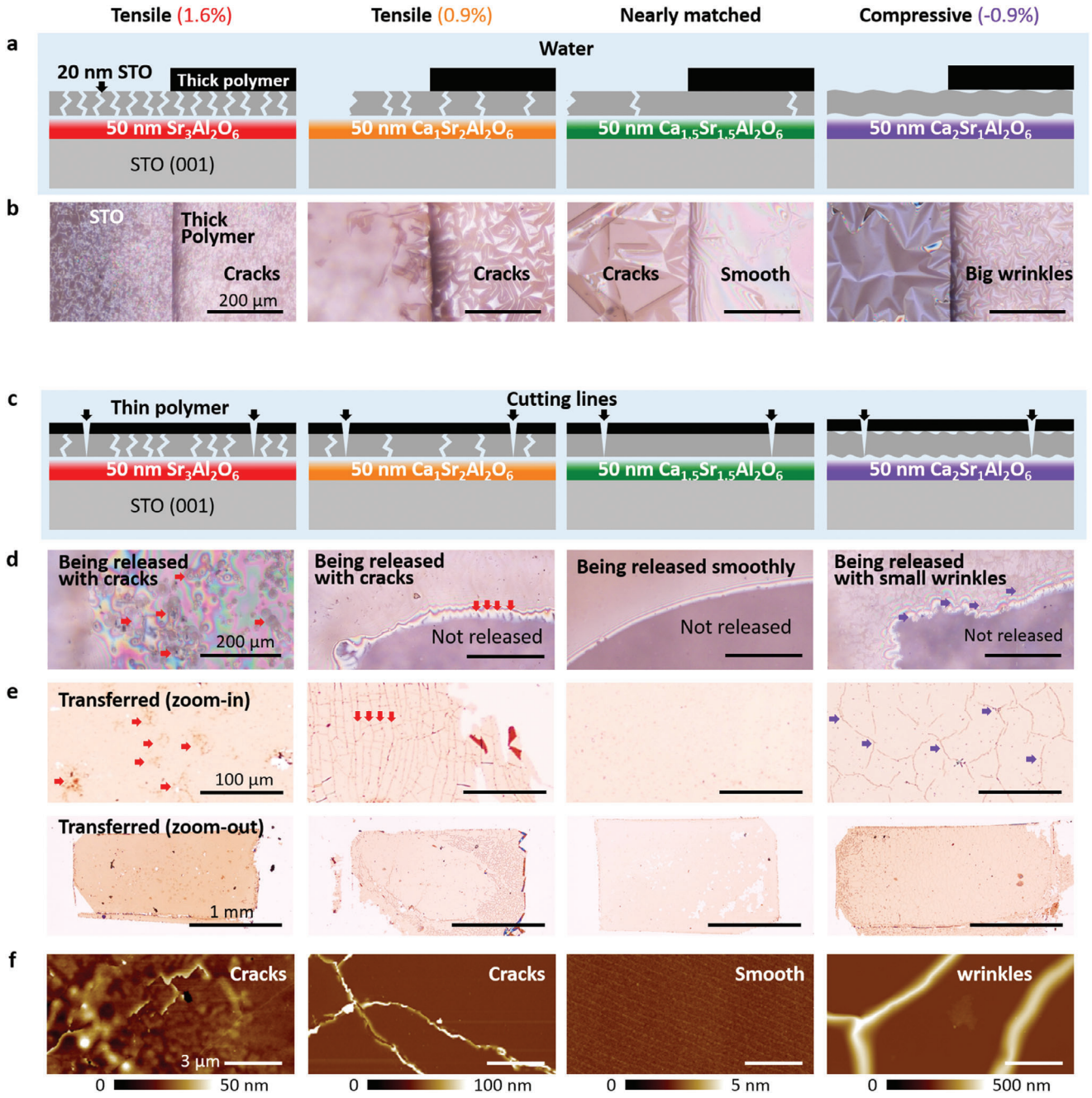

Figure 4. provides a detailed examination of the STO release process when the underlying CSAO layers are dissolved in water. a) Schematics that depict the features of the released STO layer situated beneath a thick polymer when immersed in water. b) Microscopic images of areas both with and without the polymer, provide a visual representation of the STO layers' release features as described in section (a). c) Schematics that illustrate the features of the released STO layer when it is positioned beneath a thin polymer. d) Microscopic images capture the STO layers' release features during their immersion in water, corresponding to the schematics in section (c). e) Display microscopic images of the transferred STO layers onto Si substrates. Upper images provide a more detailed, close-up perspective, while bottom images offer a broader view. f) The surface topographies measured by AFM on each transferred layers.

released from the dissolved CSAO. As illustrated in Figure 4a,b, numerous cracks form in the STO layer released from SAO, which has a 1.6% tensile strain. In contrast, the STO with a 0.9% tensile strain exhibits fewer cracks. STO layers that are nearly matched with CSAO release smoothly in water, attributed to minimal changes in the strain state before and after the release. Conversely, compressively strained STO on CSAO, with a strain of −0.9%, develops wrinkles as its lattice parameters expand during the release. When the polymer thickness is minimal (≈5 μm) in Fgure 4c,d, a low-elasticity polymer can either stretch or compress, adapting to the changes in the STO layer during its release. This results in fewer cracks and narrower wrinkles in the

released layer compared to when supported by a thicker polymer. In Figure 4d, cracks and wrinkles are highlighted by red and purple arrows, respectively. A smooth dissolution front is evident for STO on $Ca_{1.5}Sr_{1.5}Al_2O_6$, lacking any cracks or wrinkles (watch Video S1, Supporting Information). The microscopic images in Figure 4e,f display transferred STO layers on Si substrates and their surface topographies, respectively. Here, cracks and wrinkles are prominently visible, except for the nearly matched strain where clear step-terraces appear. This underscores the importance of minimizing strain to achieve a freestanding layer that is free from cracks and wrinkles. On the other hand, it takes longer release time for the more Ca-doped SAO due to the stronger Ca—O bonding compared to Sr—O, which is shown in Figure S1 (Supporting Information). Interestingly, the highest doping of Ca, which is $Ca_2Sr_1Al_2O_6$, deviates from the tendency with an even shorter release time than $Ca_{1.5}Sr_{1.5}Al_2O_6$. We regard that this deviation might be related to the wrinkles that could accelerate the dissolving of the water-soluble layer.

The release procedure we have introduced holds significant promise in addressing the challenges of wrinkle and crack formation within freestanding membranes. By harnessing strain engineering during the growth phase and refining the wet transfer process, we can substantially reduce the onset of wrinkles and cracks. Incorporating additional measures, such as heating the material in a controlled setting and designing devices to distribute strain uniformly, can further mitigate the formation of localized cracks and wrinkles. It is crucial to recognize that this field of research is continually evolving and requires adjustment when new and novel materials are introduced.

3. Conclusion

To achieve the release of perovskite oxide films without the hindrance of cracks and wrinkles, we employed strain engineering, adjusting the lattice parameter of the water-soluble CSAO layer, and controlling the releasing time and polymer thickness. We have optimized the PLD conditions to enhance the crystal quality of the epitaxially grown layers, with the conditions varying based on the Ca doping ratio. The strain values for STO layers on SAO, $Ca_1Sr_2Al_2O_6$, $Ca_{1.5}Sr_{1.5}Al_2O_6$, and $Ca_2Sr_1Al_2O_6$ are 1.6%, 0.9%, ≈0%, and −0.9%, respectively. Notably, our findings reveal that the nearly matched strain on $Ca_{1.5}Sr_{1.5}Al_2O_6$ is optimal for producing an undamaged STO freestanding layer devoid of cracks and wrinkles. Tensile-strained STO layers tend to form cracks due to shrinkage during the release process, while compressively strained STO layers develop wrinkles owing to layer expansion. This foundational principle is versatile and can be adapted for various selectively sacrificial layers, paving the way for the development of millimeter-sized freestanding oxide devices.

4. Experimental Section

Fabrication of Epitaxial STO and CSAO Layers by PLD: Epitaxial $SrTiO_3$ (STO) and $Ca_xSr_{3-x}Al_2O_6$ (CSAO) layers were grown on single-crystal (001)-oriented STO (Shinkosha Co. Ltd.) terminated with TiO_2 using pulsed laser deposition (PLD), which is operated with a KrF ($\lambda = 248$ nm) excimer laser. The polycrystalline CSAO targets for PLD depositions were prepared by grinding and pressing $SrCO_3$, $CaCO_3$, and Al_2O_3 powders into a pellet, followed by sintering at 1350°C for 20 h. Post-sintering, these targets were examined using XRD to ensure phase purity. The $Sr_3Al_2O_6$ (SAO) targets, sourced from a commercial supplier (99.99% purity, MTI Corporation), were also analyzed by XRD upon receipt. CSAO sacrificial layers were initially deposited on STO (001) substrates at 750°C in an environment of an oxygen pressure of 10^{-5} mbar. A 20-nm-thick STO layer was grown on the CSAO layer at 700°C at the oxygen pressure of 5×10^{-4} mbar. Various laser energy densities and repetition rates were used for both STO and CSAO, as shown in Figures 1d and **2**. By reflection high-energy electron diffraction (RHEED), growth modes were monitored to determine the layer-by-layer mode and the thickness of the films through the oscillations of the RHEED spots. If RHEED oscillations were not clear enough to determine thickness during deposition, we relied on monitoring the layer's thickness through a calibrated growth rate, measured in nanometers per second, specific to each deposition.

Structural Analysis of the As-Grown Layers Using XRD: The strains of as-grown STO layers on CSAO layers were examined by an X-ray diffractometer (Rigaku SmartLab) with Cu Kα radiation (1.5406 Å). *c*-axis lattice parameters of STO and CSAO layers were calculated from the peak positions of out-of-plane (θ–2θ) scans. In the study, it is observed that only the Sr+Ca:Al = 3:2 phase in the θ–2θ scans, grown under a low oxygen pressure of 10^{-5} mbar. Notably, at a much higher pressure of ≈10^{-1} mbar (four orders of magnitude greater), the Sr+Ca:Al = 4:2 phase becomes stable, exhibiting longer lattice parameters than the 3:2 phases. For the SAO (3:2) phase, it would expect that the (002) Bragg peak at ≈45.8°, whereas for the $Sr_4Al_2O_7$ (4:2) phase, it should appear near 41.8°. In the experiments, only the peak ≈45.8°is detected and observed no peaks near 41.8°, confirming the stability of the $Sr_3Al_2O_6$ phase in the experimental conditions. *a*-axis lattice parameters and strain values were deduced from the peak positions of 103 reflections in the reciprocal space maps (RSMs).

Fabrication of Freestanding Membrane by Transfer: STO membranes were transferred onto the Si substrates by releasing the membranes in the DI water at room temperature. To support STO membranes in the water, ≈100-µm-thick and ≈5-µm-thick cellulose acetate butyrate (CAB) were used as support layers before immersing the epitaxial STO films in the water.[2] To make a ≈100-µm-thick CAB layer (≈5-µm-thick CAB layer), 20 g CAB in 100 mL of ethyl acetate was spin-coated on Si substrate at 1000 rpm (3000 rpm) for the 60 s. After covering the sample with a CAB layer and annealing, to make water penetrate the CSAO layers, the CAB layers were cut with straight lines parallel to crystal edges. The release time for 50-nm-thick CSAO ranges from ≈20 min to 10 h, depending on the doping ratio in DI water at room temperature (see Figure S1, Supporting Information). Once the STO membranes with CAB layers are fully released, the floating membranes are scooped by the Si substrate. After thoroughly drying DI water at room temperature for good adhesion, the CAB layers were removed by acetone and followed by IPA.

Supporting Information

Supporting Information is available from the Wiley Online Library or from the author.

Acknowledgements

N.P. and E.B. acknowledge the support of Novo Nordisk Foundation Challenge Pro-gramme 2021: Smart nanomaterials for applications in life-science, BIOMAG Grant NNF21OC0066526. N.P., S.Y., and C.H. acknowledge the support from the ERC Advanced "NEXUS" Grant 101054572, and N.P. acknowledge the Danish Council for Independent Research Technology and Production Sciences for the DFF- Research Project 3 (grant No 00069B).

Conflict of Interest

The authors declare no conflict of interest.

Data Availability Statement

The data that support the findings of this study are available from the corresponding author upon reasonable request.

Keywords

cracks, freestanding, oxide thin film, release, strain, transfer, wrinkles

Received: November 22, 2023
Revised: January 30, 2024
Published online:

[1] D. Lu, D. J. Baek, S. S. Hong, L. F. Kourkoutis, Y. Hikita, H. Y. Hwang, *Nat. Mater.* **2016**, *15*, 1255.
[2] Y. Li, C. Xiang, F. M. Chiabrera, S. Yun, H. Zhang, D. J. Kelly, R. T. Dahm, C. K. R. Kirchert, T. E. Le Cozannet, F. Trier, D. V. Christensen, T. J. Booth, S. B. Simonsen, S. Kadkhodazadeh, T. S. Jespersen, N. Pryds, *Adv. Mater.* **2022**, *34*, 2203187.
[3] A. Brewer, S. Lindemann, B. Wang, W. Maeng, J. Frederick, F. Li, Y. Choi, P. J. Thompson, J. W. Kim, T. Mooney, V. Vaithyanathan, D. G. Schlom, M. S. Rzchowski, L. Q. Chen, P. J. Ryan, C. B. Eom, *Appl. Phys. Lett.* **2021**, *119*, 202903.
[4] R. Xu, K. J. Crust, V. Harbola, R. Arras, K. Y. Patel, S. Prosandeev, H. Cao, Y.-T. Shao, P. Behera, L. Caretta, W. J. Kim, A. Khandelwal, M. Acharya, M. M. Wang, Y. Liu, E. S. Barnard, A. Raja, L. W. Martin, X. W. Gu, H. Zhou, R. Ramesh, D. A. muller, L. Bellaiche, H. Y. Hwang, *Adv. Mater.* **2023**, *35*, 2210562.
[5] V. Harbola, R. Xu, S. Crossley, P. Singh, H. Y. Hwang, *Appl. Phys. Lett.* **2021**, *119*, 053102.
[6] M. Sheeraz, M.-H. Jung, Y. K. Kim, N.-J. Lee, S. Jeong, J. S. Choi, Y. J. Jo, S. Cho, I. W. Kim, Y.-M. Kim, S. Kim, C. W. Ahn, S. M. Yang, H. Y. Jeong, T. H. Kim, *ACS Nano* **2023**, *17*, 13510.
[7] R. Yu, L. Gong, H. Ohta, T. Katayama, *A.C.S. Appl., Electron. Mater.* **2023**, *5*, 5234.
[8] K. T. Kang, Z. J. Corey, J. Hwang, Y. Sharma, B. Paudel, P. Roy, L. Collins, X. Wang, J. W. Lee, Y. S. Oh, Y. Kim, J. Yoo, J. Lee, H. Htoon, Q. Jia, A. Chen, *Adv. Sci.* **2023**, *10*, 2207481.
[9] D. Ji, S. Cai, T. R. Paudel, H. Sun, C. Zhang, L. Han, Y. Wei, Y. Zang, M. Gu, Y. Zhang, W. Gao, H. Huyan, W. Guo, D. Wu, Z. Gu, E. Y. Tsymbal, P. Wang, Y. Nie, X. Pan, *Nature* **2019**, *570*, 87.
[10] Q. Lu, Z. Liu, Q. Yang, H. Cao, P. Balakrishnan, Q. Wang, L. Cheng, Y. Lu, J.-M. Zuo, H. Zhou, P. Quarterman, S. Muramoto, A. J. Grutter, H. Chen, X. Zhai, *ACS Nano* **2022**, *16*, 7580.
[11] H. Elangovan, M. Barzilay, S. Seremi, N. Cohen, Y. Jiang, L. W. Martin, Y. Ivry, *ACS Nano* **2020**, *14*, 5053.
[12] G. Dong, S. Li, M. Yao, Z. Zhou, Y. Q. Zhang, X. Han, Z. Luo, J. Yao, B. Peng, Z. Hu, H. Huang, T. Jia, J. Li, W. Ren, Z. G. Ye, X. Ding, J. Sun, C. W. Nan, L. Q. Chen, J. Li, M. Liu, *Science* **2019**, *366*, 475.
[13] B. Peng, R. C. Peng, Y. Q. Zhang, G. Dong, Z. Zhou, Y. Zhou, T. Li, Z. Liu, Z. Luo, S. Wang, Y. Xia, R. Qiu, X. Cheng, F. Xue, Z. Hu, W. Ren, Z. G. Ye, L. Q. Chen, Z. Shan, T. Min, M. Liu, *Sci. Adv.* **2020**, *6*, eaba5847.
[14] C. Jin, Y. Zhu, X. Li, F. An, W. Han, Q. Liu, S. Hu, Y. Ji, Z. Xu, S. Hu, M. Ye, G. Zhong, M. Gu, L. Chen, *Adv. Sci.* **2021**, *8*, 2102178.
[15] S. S. Hong, M. Gu, M. Verma, V. Harbola, B. Y. Wang, D. Lu, A. Vailionis, Y. Hikita, R. Pentcheva, J. M. Rondinelli, H. Y. Hwang, *Science* **2020**, *368*, 71.
[16] R. Xu, J. Huang, E. S. Barnard, S. S. Hong, P. Singh, E. K. Wong, T. Jansen, V. Harbola, J. Xiao, B. Y. Wang, S. Crossley, D. Lu, S. Liu, H. Y. Hwang, *Nat. Commun.* **2020**, *11*, 3141.
[17] G. Dong, S. Li, T. Li, H. Wu, T. Nan, X. Wang, H. Liu, Y. Cheng, Y. Zhou, W. Qu, Y. Zhao, B. Peng, Z. Wang, Z. Hu, Z. Luo, W. Ren, S. J. Pennycook, J. Li, J. Sun, Z. G. Ye, Z. Jiang, Z. Zhou, X. Ding, T. Min, M. Liu, *Adv. Mater.* **2020**, *32*, 2004477.
[18] J. Liu, Y. Feng, R. Tang, R. Zhao, J. Gao, D. Shi, H. Yang, *Adv. Electron. Mater.* **2018**, *4*, 1700522.
[19] F. M. Chiabrera, S. Yun, Y. Li, R. T. Dahm, H. Zhang, C. K. R. Kirchert, D. V. Christensen, F. Trier, T. S. Jespersen, N. Pryds, *Ann. Phys.* **2022**, *534*, 2200084.
[20] Q. Wang, H. Fang, D. Wang, J. Wang, N. Zhang, B. He, W. Lu, *Crystals* **2020**, *10*, 733.
[21] L. Gong, M. Wei, R. Yu, H. Ohta, T. Katayama, *ACS Nano* **2022**, *16*, 21013.
[22] R. Li, Y. Xu, J. Song, P. Wang, C. Li, D. Wu, *Appl. Phys. Lett.* **2020**, *116*, 222904.
[23] Y. Zhao, R. Peng, Y. Guo, Z. Liu, Y. Dong, S. Zhao, Y. Li, G. Dong, Y. Hu, J. Zhang, Y. Peng, T. Yang, B. Tian, Y. Zhao, Z. Zhou, Z. Jiang, Z. Luo, M. Liu, *Adv. Funct. Mater.* **2021**, *31*, 2009376.
[24] T. Wang, R. C. Peng, W. Peng, G. Dong, C. Zhou, S. Yang, Z. Zhou, M. Liu, *Adv. Funct. Mater.* **2021**, *32*, 2108496.
[25] K. Gu, T. Katayama, S. Yasui, A. Chikamatsu, S. Yasuhara, M. Itoh, T. Hasegawa, *Adv. Funct. Mater.* **2020**, *30*, 2001236.
[26] P. Su, H. Wen, Y. Zhang, C. Tan, X. Zhong, Y. Wu, H. Song, Y. Zhou, Y. Li, M. Liu, J. Wang, *ACS Appl. Electron. Mater.* **2022**, *4*, 2987.
[27] Y. Guo, B. Peng, R. Qiu, G. Dong, Y. Yao, Y. Zhao, Z. Zhou, M. Liu, *Adv. Func. Mater.* **2023**, *33*, 2213668.
[28] S.-I. Kim, H.-J. Choi, G. Lee, C. J. Roh, I. Jung, S. Y. Jung, R. Ning, S. O. Won, H. J. Chang, J. S. Lee, S. K. Kim, J.-S. Kim, C.-Y. Kang, J.-W. Choi, S.-H. Baek, *Mater. Horiz.* **2020**, *7*, 1552.
[29] D. Kim, M. Kim, S. Reidt, H. Han, A. Baghizadeh, P. Zeng, H. Choi, J. Puigmartí-Luis, M. Trassin, B. J. Nelson, X.-Z. Chen, S. Pané, *Nat. Commun.* **2023**, *14*, 750.
[30] X. Li, *J. Phys. D: Appl. Phys.* **2008**, *41*, 193001.
[31] I. S. Chun, X. Li, *IEEE Trans. Nanotechn.* **2008**, *7*, 493.
[32] S. Lee, F. Nagata, K. Kato, T. Nakano, T. Kasuga, *Materials* **2021**, *14*, 1736.